Article

Not peer-reviewed version

Intrinsic Equations and High-Temperature Heat Distortion Behavior of TA4 Alloy

Lifeng Ma , Wenshuai Liu , Yanchun Zhu * , Ling Qin , Jingfeng Zhou

Posted Date: 24 February 2025

doi: 10.20944/preprints202502.1880.v1

Keywords: TA4 alloy; Hot deformation behavior; Hot processing map; Thermal deformation mechanism; EBSD

Preprints.org (www.preprints.org) | NOT PEER-REVIEWED | Posted: 24 February 2025 doi:10.20944/preprints202502.1880.v1

Article

Intrinsic Equations and High-Temperature Heat Distortion Behavior of TA4 Alloy

Lifeng Ma [1], Wenshuai Liu [1], Yanchun Zhu [1,*] , Ling Qin [2], Jingfeng Zou [1]

[1] School of Mechanical Engineering, Taiyuan University of Science and Technology, Taiyuan 030024, China
[2] Department of Petroleum Engineering, University of Wyoming, Laramie, WY, 82071, USA
* Correspondence: lzlzyc@163.com

Abstract: In this study, the high-temperature thermal deformation behavior of TA4 alloy was investigated through thermal compression experiments. The effects of deformation temperature and strain rate on rheological stress were analyzed by examining the variations in stress-strain curves under different conditions and establishing a constitutive equation based on the dynamic material theory model. The prediction accuracy of the developed constitutive model was evaluated, yielding a correlation coefficient of 0.9612 between predicted and experimental values, an average absolute percentage error of 8.7210%, and an average root mean square error of 11.0635 MPa. Thermal processing diagrams were established and plotted to analyze the optimal processing zone and the destabilization zone under different strains. The optimal processing zones at different strains are obtained from the thermal processing diagrams, which are 1040~1133K, 0.01~0.7s^{-1} at a strain of 0.9, 940~1000K, 0.01~0.04 s^{-1} at a strain of 0.6, 940~1000K, 0.01~0.08s^{-1} at a strain of 0.3, 940~1000K, 0.01~0.08s^{-1} at a strain of 0.3. Additionally, the thermal deformation mechanisms of TA4 alloy under varying deformation parameters were analyzed using EBSD characterization. The results indicate that the primary deformation softening mechanisms include dynamic recovery (DRV) at low temperatures and high strain rates, dynamic recrystallization (DRX) at high temperatures and high strain rates, and DRX at low strain rates.

Keywords: TA4 alloy; Hot deformation behavior; Hot processing map; Thermal deformation mechanism; EBSD

---

1. Introduction

Titanium, known as the "third metal" after iron and aluminum due to its abundant reserves in the Earth's crust, has garnered significant attention. Titanium alloys, owing to their excellent comprehensive properties such as high specific strength, low density, low thermal expansion coefficient, high biocompatibility, and high corrosion resistance, are widely used in aerospace, petrochemical, automotive, shipbuilding, and biomedical fields[1-3]. In recent years, titanium alloys have gained strong momentum in the civil market, particularly as materials for consumer electronics. They have already been commercialized in electronic fabrication and aerospace industrial applications.

During the hot deformation process, the machinability of titanium alloys is influenced by both deformation parameters and material microstructure. Therefore, selecting appropriate deformation parameters such as strain rate, strain, and deformation temperature is crucial for the processing and mechanical performance of the final product[4,5]. These parameters interact with each other and jointly influence the hot mechanical processing of titanium alloys[6]. A constitutive model can be developed to represent the relationship between stress and strain under different loads, as well as to predict the hot processing performance under various deformation parameters. Additionally, the use of hot processing maps allows for a more accurate determination of the material's processing window, providing guidance for the optimization of deformation parameters during hot processing.

Yu et.al[7] conducted high-temperature compression experiments on near-α titanium alloys, studying their high-temperature deformation behavior, microstructural evolution, and hot processing maps. Wang et.al [8] used isothermal compression testing on Ti-55511 titanium alloy to investigate the effects of various hot deformation parameters on the alloy's properties and microstructural evolution. Lu et.al [9] analyzed the flow stress-strain curves of TA10 titanium alloy under different strain rates and temperatures and developed a high-temperature plasticity constitutive equation for pure titanium alloy based on a hyperbolic sine Arrhenius equation. Furthermore, the microstructural evolution behavior during processing, such as dynamic recrystallization and dynamic recovery, inevitably impacts the machinability of the final product. Therefore, studying the influence of different deformation parameters on microstructural evolution during hot processing is essential for further exploring suitable manufacturing processes for TA4 titanium alloy[10,11].

Over the past few years, our group have explored a diverse range of alloy systems, including, but not limited to, nickel-based superalloys and aluminum alloys[12-20]. In this study, the high-temperature deformation behavior of TA4 titanium alloy was investigated through high-temperature compression tests. A high-temperature plasticity constitutive equation was developed using the hyperbolic sine Arrhenius equation and the dynamic material theory model, and hot processing maps were generated across various strain levels. The predictive accuracy of the constitutive equation was quantitatively evaluated using correlation coefficients (R), mean absolute percentage error (MAPE), and root mean square error (RMSE). Additionally, the constitutive equation and hot processing maps were applied to identify and mitigate potential processing defects during the hot working of TA4 alloy. Furthermore, the influence of titanium alloys on microstructural evolution, including dynamic recrystallization and dynamic recovery under different processing parameters, was also examined.

2. Materials and Methods

The experimental material used in this study is commercial-grade TA4 titanium wire, supplied by Puying Metal Materials Technology Co., Ltd. The wire underwent multiple vacuum remelting, followed by forging and high-line rolling. TA4 titanium alloy is an α-type titanium alloy, and after annealing, its microstructure consists predominantly of equiaxed α phase, with a small amount of β phase (dark regions) present at the grain boundaries. Figure 1 illustrates the original microstructure of the alloy, which is largely recrystallized, featuring equiaxed α phase with a relatively uniform grain size, averaging approximately 10 μm. Table 1 presents the elemental composition and content of the TA4 titanium alloy used in the experiment.

Table 1. Chemical composition of the TA4 titanium alloy (%,wt).

Fe	C	N	H	H	Ti
0.15	0.05	0.007	0.0021	0.0021	Bal.

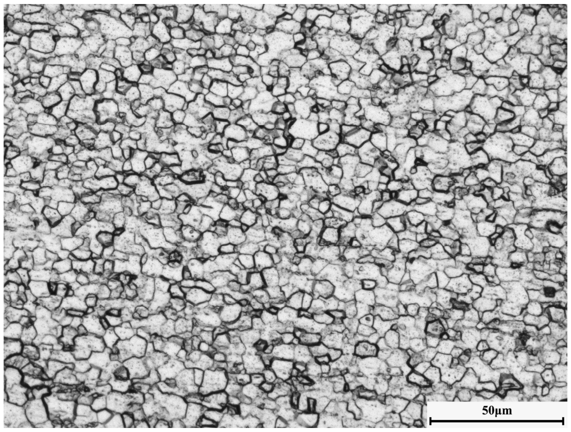

Figure 1. Microstructure of the TA4 titanium alloy.

High-temperature compression tests were conducted using a Gleeble-3800 thermo-mechanical simulator. The samples used in the experiments were TA4 alloy rods with dimensions of ϕ8.0 mm × ϕ12.0 mm. The experimental procedure is shown in Fig 2. The deformation temperatures of the samples were set at 660°C,710°C, 760°C, 810°C, and 860°C, with a deformation degree of 60%. The deformation rates were 0.01 s^{-1}, 0.1 s^{-1}, 1 s^{-1}, and 10 s^{-1}. During the experiment, the samples were heated at a rate of 10°C/s to the specified compression deformation temperature and held at that temperature for 3 minutes to ensure uniform temperature distribution within the sample. The sample was then compressed to 60% strain at the specified constant strain rate, and water cooling was applied after the compression. At the end of the experiment, the load and displacement during compression were recorded by the analog testing machine through the force sensor and displacement sensor, and the stress-strain curve was generated.

To minimize the influence of friction on the experiment, lubricant was applied to both ends of the sample in contact with the Gleeble-3800 simulator, and graphite sheets were attached. Additionally, the chamber was vacuumed and protected with gas before the experiment. To maintain uniform temperature during the entire high-temperature compression process, a pair of S-type Pt/Rh thermocouples were spot-welded at the midpoint along the height of the sample. The force and displacement sensors in the simulator actively collected the load and displacement during deformation, and the internal program automatically converted these measurements into true stress-true strain curves.

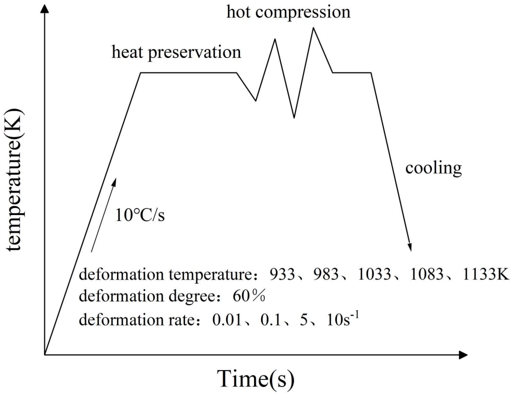

Figure 2. Heat compression experimental process.

3. Results

3.1. Flow Stress Behavior

The mechanism of titanium alloy hot deformation is typically observed through true stress-strain curves. The true stress-strain curves of TA4 titanium alloy under different deformation conditions are shown in Figure 3. From the figure, it can be observed that the flow stress of TA4 titanium alloy generally increases rapidly at first and then stabilizes under different stress-strain curves. This is because, in the initial stage of compression, the alloy undergoes intense work hardening, leading to a rapid increase in flow stress, which is reflected in the continuous rapid increase in flow stress on the stress-strain curve. As compression time increases, softening mechanisms such as dynamic recovery and dynamic recrystallization begin to take effect. When a stable state is reached, these two effects counteract each other, resulting in the flow stress stabilizing[21,22].

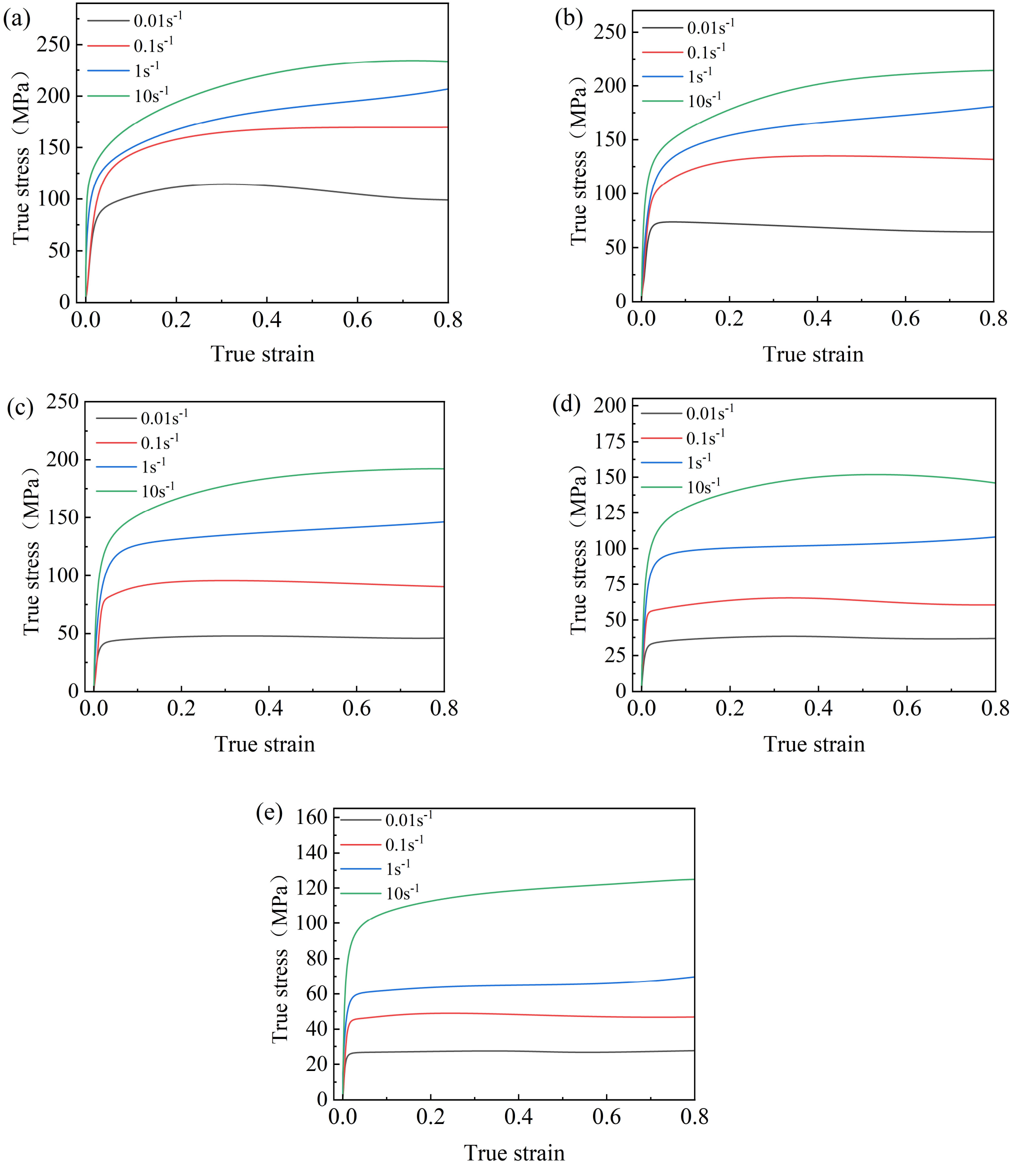

Figure 3. When the strain rate is between 0.001s^{-1} and 10s^{-1}, the true stress-strain curves of TA4 alloy at different deformation temperatures are as follows: (a)933K，(b) 983K，(c) 1033K，(d) 1083K，(e) 1133K.

Figure 4 shows the peak stress values of TA4 titanium alloy at different deformation parameters, in which it can be seen that the peak stress of the material decreases significantly with increasing deformation temperature and decreasing strain rate. At 933 K, the peak stress increases from 110.42 MPa at strain rate 0.01s^{-1} to 235.27 MPa at 10s^{-1} , which is an increase of 113%; at 983 K, the peak stress increases from 73.64 MPa at 0.01s^{-1} to 214.28 MPa at 10s^{-1} , which is an increase of 190%; at 1033 K, the peak stress increases from 47.57 MPa at 0.01s^{-1} to 192.26 MPa at 10s^{-1}, an increase of 304%; at 1083 K, the peak stress increases from 38.32 MPa at 0.01s^{-1} to 151.89 MPa at 10s^{-1}, an increase of 296%; at 1133 K, the peak stress increases from 38.32 MPa at 0.01s^{-1} to 151.89 MPa at 10s^{-1}, an increase of 296%; at 1133 K, the peak stress increases from 38.32 MPa at 0.01s^{-1} to 151.89 MPa at 10s^{-1}, an increase of 296%. at 1133 K. The peak stress increases from 38.32MPa at 0.01s^{-1} to 151.89MPa at 10s^{-1}, an increase of 340%. From the analysis, it was found that firstly, the strain rate is proportional to the peak stress at the same deformation temperature. This is because the compression time of the material becomes shorter when the strain rate increases. When the deformation time of the material is not enough to allow the softening mechanisms such as dynamic restitution and dynamic recrystallization within the alloy to be fully activated, this is manifested by an increase in peak stress. Secondly, at lower temperatures (below 1033 K), the increase in peak stress with increase in strain rate is relatively modest, 113% versus 190%, respectively. This indicates that the change in strain rate at low temperature has less effect on the heat distortion process of TA4 titanium alloy. At higher temperatures (above 1033 K), the increase in peak stress rises to 304%, 296% and 340%. This indicates that the thermal deformation process of the material becomes more sensitive to the strain rate with increasing temperature. This is due to the fact that the higher the deformation temperature of the alloy, the higher the dislocation activity of the alloy, resulting in a higher deformation storage energy. At the same time, the nucleation and growth of dynamically recrystallized grains are more rapid with increasing temperature, leading to an increase in the softening mechanism of the alloy and a consequent decrease in its resistance to deformation.

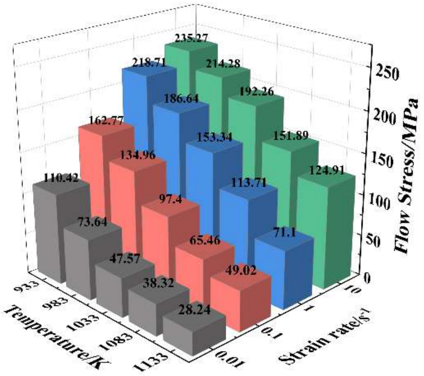

Figure 4. Peak stresses of alloys at different deformation conditions.

3.2. Derivation of the Constitutive Equation

To study the relationship between stress, strain, and temperature during the deformation of metallic materials, a constitutive equation must be developed for the material. The Arrhenius model is commonly used to construct the constitutive equation for the hot deformation behavior of titanium alloys. This hyperbolic sine constitutive model is not only widely applicable but also offers high predictive accuracy. Considering these factors, this model was selected to construct the constitutive equation for TA4 alloy at a strain of 0.5. The mathematical expression of this equation consists of three equations, as shown in Equation (1)[23-25]:

$$\dot{\varepsilon} = \begin{cases} A_1\sigma^{n_1}\exp\left(-\frac{Q}{RT}\right) & (\alpha\sigma < 0.8) \\ A_2\exp(\beta\sigma)\exp\left(-\frac{Q}{RT}\right) & (\alpha\sigma > 1.2) \\ A_3[\sinh(\alpha\sigma)]^{n_2}\exp\left(-\frac{Q}{RT}\right) & (for\ all) \end{cases} \tag{1}$$

In Eq. (1), $\dot{\varepsilon}$ is the strain rate; σ can represent the peak stress, steady state variable rheological stress, or the rheological stress of the specified strain; n_1、n_2 are temperature-independent stress indices; A_1 , A_2 , A_3 , and β are material constants that are also temperature-independent; Q is the apparent activation energy of thermal deformation at different temperatures; T is the thermodynamic temperature at absolute temperature; R is the gas constant in the ideal state; α is a parameter characterizing the pressure level, and the relationship with other parameters is $\alpha = \beta/n$.

It has been shown that the third equation is usually used to construct the eigenequations for different stress conditions. The hyperbolic sine form was proposed by Sellars and Mc Tegart, which can express the eigenequations more accurately under different stress conditions. It is well adapted for use and widely used, and is expressed as follows:

$$\dot{\varepsilon} = A_3[\sinh(\alpha\sigma)]^{n_2}\exp\left(-\frac{Q}{RT}\right) \tag{2}$$

The Zener-Hollomon parameter Z[26], which expresses the relationship between the strain rate $\dot{\varepsilon}$ and the absolute temperature T, was used as follows:

$$Z = \dot{\varepsilon}exp\left(\frac{Q}{RT}\right) \tag{3}$$

According to equations (2) and (3):

$$Z = A_3[\sinh(\alpha\sigma)]^n \tag{4}$$

Equation (4) where Z is the deformation rate factor for temperature compensation. The meanings of the other letters have been pointed out above.

According to the definition of hyperbolic sine function has:

$$\sinh^{-1}(\alpha\sigma) = \left[\ln(\alpha\sigma) + ((\alpha\sigma)^2 + 1)^{\frac{1}{2}}\right] \tag{5}$$

According to equations (3), (4), and (5), it can be obtained:

$$\sigma = \frac{1}{\alpha}\ln\left\{\left(\frac{Z}{A_3}\right)^{\frac{1}{n_2}} + \left[\left(\frac{Z}{A_3}\right)^{\frac{2}{n_2}} + 1\right]^{\frac{1}{2}}\right\} \tag{6}$$

The natural logarithm can be obtained by solving for each side of equation (1):

$$ln\dot{\varepsilon} = A_4 + n_1 ln\sigma \tag{7}$$

$$ln\dot{\varepsilon} = A_5 + \beta\sigma \tag{8}$$

$$ln\dot{\varepsilon} = n_2 ln[sinh(\alpha\sigma)] + A_6 \tag{9}$$

The steady state stress and strain rates during deformation were taken, and according to Eq. (7) and Eq. (8), the least squares method was adopted for the linear regression process, and the relationship between $ln\sigma - ln\dot{\varepsilon}$ and $\sigma - ln\dot{\varepsilon}$ was plotted with the help of Origin data analysis software, and the results are shown in Figure 5[27]. The fitting results show that the linear correlation coefficients of $ln\sigma - ln\dot{\varepsilon}$ curves at 1083K and 1133K and $\sigma - ln\dot{\varepsilon}$ curves at 1033K and 1083K are all greater than 0.99, indicating a good fitting reliability.

Taking the average value of the inverse of the slope of the fitted straight line in Figure 5(a) for 1083K and 1133K as n_1, there is n_1=4.9046; taking the average value of the inverse of the slope of the fitted straight line in Figure 5(b) for 1083K and 1133K as β,there is β=0.0492MPa^{-1}; and according to the definition of α, we can get $\alpha = \beta/n = 0.0101\mathrm{MP}^{-1}$.

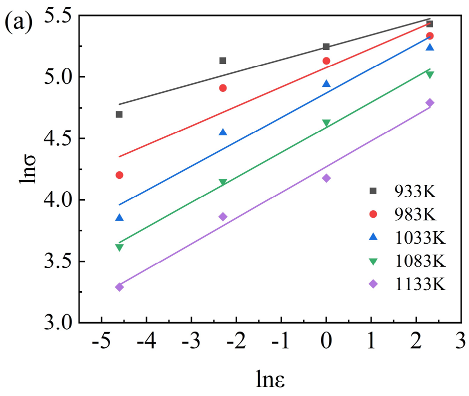

Figure 5. The relationship between rheological stress and strain rate of TA4 alloy.

(a)$\ln\ \sigma-\ln\ \dot{\varepsilon}$ (b) $\sigma-\ln\ \dot{\varepsilon}$

The strain stress and strain rate at different deformation temperatures were substituted according to Eq. (9), and the linear regression was fitted by the least-squares method, and the $\ln\left[\sinh\left(\alpha\sigma\right)\right]-ln\dot{\varepsilon}$ relationship was plotted with the help of Origin data analysis software, as shown in Figure6. The fitting results show that the linear correlation coefficients of the $\ln\left[\sinh\left(\alpha\sigma\right)\right]-ln\dot{\varepsilon}$ curves at 1033 K, 1083 K, and 1133 K are all greater than 0.99, indicating that the double logarithmic relationship between the high-temperature deformation rheological stresses and the strain rate satisfies the linear relationship better; The results show that the relationship between rheological stress and strain rate of TA4 alloy at high temperature constant deformation temperature can be described by hyperbolic sine relationship.

A certain temperature range, assuming constant Q at the same strain rate, is obtained according to (9):

$$\ln[\sinh(\alpha\sigma)]=A_7+\frac{A_8}{T} \qquad (10)$$

The strain rate $\dot{\varepsilon}$, the stress σ and the calculated α value were brought into Eq. (10), while the least squares method was taken for the linear regression treatment to plot the $\ln[\sinh(\alpha\sigma)]-\frac{1}{T}$ relationship, as shown in Figure 5. The fitting results show that the linear correlation coefficients of the $\ln[\sinh(\alpha\sigma)]-\frac{1}{T}$ curves are greater than 0.99 at all strain rates, indicating that the relationship between the rheological stress and the temperature of TA4 alloy at high temperature and constant strain rate can be described by the hyperbolic sine relationship.

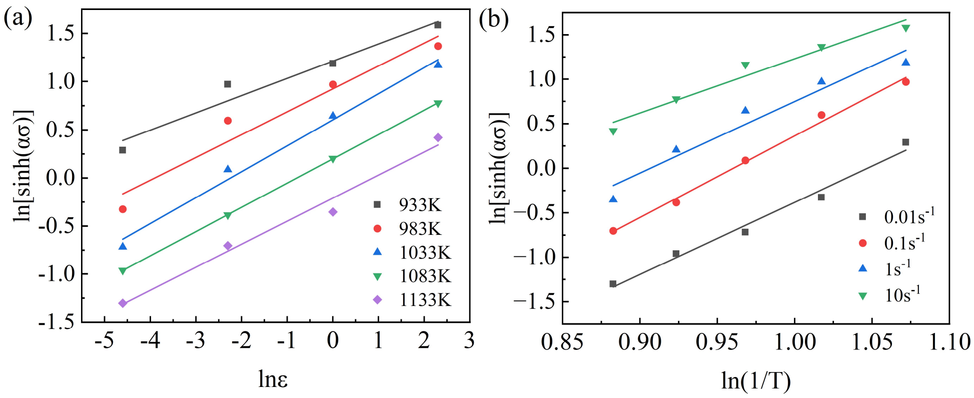

Figure 6. (a)$\ln[\sinh(\alpha\sigma)]-ln\dot{\varepsilon}$ fit curve; (b) $\ln[\sinh(\alpha\sigma)]-\frac{1}{T}$ fit curve.

Taking the natural logarithm of the derivative on both sides of the third equation of Eq. (1), the high-temperature deformation activation energy equation can be obtained as follows.

$$Q = R\left\{\frac{\partial(\ln\dot{\varepsilon})}{\partial \ln[\sinh(\alpha\sigma)]}\right\}_T \left\{\frac{\partial \ln[\sinh(\alpha\sigma)]}{\partial\left(\frac{1}{T}\right)}\right\}_\varepsilon \quad (11)$$

According to the previous calculations, the three terms on the right side of Eq. (11) are the gas constant in the ideal state, the inverse of the slope of the $\ln[\sinh(\alpha\sigma)] - \ln\dot{\varepsilon}$ curve at a certain temperature, and the slope of the $\ln[\sinh(\alpha\sigma)] - \frac{1}{T}$ curve at a certain strain rate, and the values of the latter two are 3.9634 and 9.1436, respectively. Substituting into Eq. (11) yields the value of the deformation activation energy Q as 301 KJ/mol.

Taking the logarithm of both sides of Eq. (4) can be obtained:

$$\ln Z = \ln A + n\ln[\sinh(\alpha\sigma)] \quad (12)$$

The obtained average deformation activation energy Q value, strain rate and deformation temperature were substituted into Eq. (12), and the plot of $\ln Z - \ln[\sinh(\alpha\sigma)]$ relationship plotted by linear regression using the least squares method is shown in Figure 7. Since the linear correlation coefficient between the variables of the relationship plot is greater than 0.98, the stress index n can be expressed by the slope of this fitted curve, and $\ln A$ can be expressed by the intercept. The data processing can get $n = 4.2924$ and $A = 1.9653 \times 10^{14}\text{s}^{-1}$.

Combined with the above calculation results, all the material parameters for constructing the constitutive equation of TA4 alloy have been found out, which are: stress level factor $\alpha = 0.0101\text{MP}a^{-1}$, activation energy of deformation $Q = 301\text{KJ/mol}$, stress exponent $n = 4.2923$, and structure factor $A = 1.9654 \times 10^{14}s^{-1}$, respectively. Substituting the above parameters into Eq. (2), the eigenstructural equation for a strain of 0.5 temperature range of 933-1133 K can be found as:

$$\dot{\varepsilon} = 1.9654 \times 10^{14}[sinh(0.0101\sigma)]^{4.2923} \exp\left(\frac{-301000}{RT}\right) \quad (13)$$

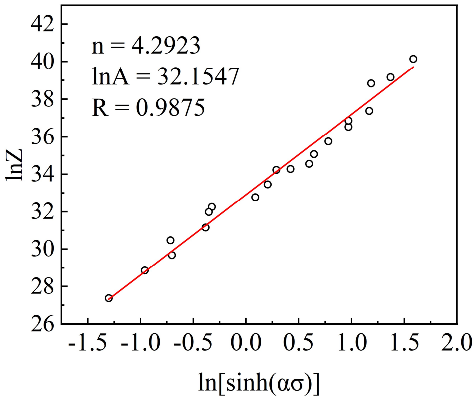

Figure 7. Relationship diagram of lnZ − ln[sinh (ασ)] TA4 alloy.

Similarly, the parameter data of Arrhenius model for different strain ranges and different deformation conditions can be calculated by the above method, as shown in Table 2.

Table 2. Arrhenius model parameter.

material Constant	strain rate							
	0.1	0.2	0.3	0.4	0.5	0.6	0.7	0.8
α	0.0119	0.0112	0.0107	0.0105	0.0105	0.0105	0.0105	0.0105
Q	317.1401	320.5820	315.5531	304.7553	295.4912	283.9743	276.3184	272.3312
n	5.5782	5.1983	4.9145	4.6582	4.4234	4.2371	4.0892	4.0433
ln A	34.2532	34.7864	34.3312	33.1813	32.1540	30.8460	29.9552	29.4720

However, Bani et.al[28] argued that the important effect of strain on this process should be taken into account when analyzing the high temperature deformation of titanium alloys. The results showed that strain has a significant effect on the deformation activation energy and material constants (α, n, Q and lnA). Therefore, in order to investigate the intrinsic modeling of titanium alloys under different strains, the relationship of strain on deformation activation energy and material constants is constructed as a polynomial function as shown in Eq. (14). The effect of strain on the constitutive equation is reflected by the application of the polynomial function in the constitutive equation.

$$\begin{cases} \alpha = C_0 + C_1\varepsilon + C_2\varepsilon^2 + C_3\varepsilon^3 + C_4\varepsilon^4 + C_5\varepsilon^5 \\ Q = E_0 + E_1\varepsilon + E_2\varepsilon^2 + E_3\varepsilon^3 + E_4\varepsilon^4 + E_5\varepsilon^5 + E_6\varepsilon^6 \\ n = D_0 + D_1\varepsilon + D_2\varepsilon^2 + D_3\varepsilon^3 + D_4\varepsilon^4 + D_5\varepsilon^5 + D_6\varepsilon^6 \\ lnA = F_0 + F_1\varepsilon + F_2\varepsilon^2 + F_3\varepsilon^3 + F_4\varepsilon^4 + F_5\varepsilon^5 + F_6\varepsilon^6 \end{cases} \quad (14)$$

According to Eq. (14), the correlations of $\alpha - \varepsilon, n - \varepsilon, Q - \varepsilon$ and $lnA - \varepsilon$ are plotted, and the fitted curves are shown in Figure 8. From the figure, it can be found that the correlation coefficients of each fitted curve of strain versus material constants are greater than 0.99, which has a good reliability. It indicates that this polynomial function can be used to describe the strain-to-material constant relationship during high temperature deformation of titanium alloy.

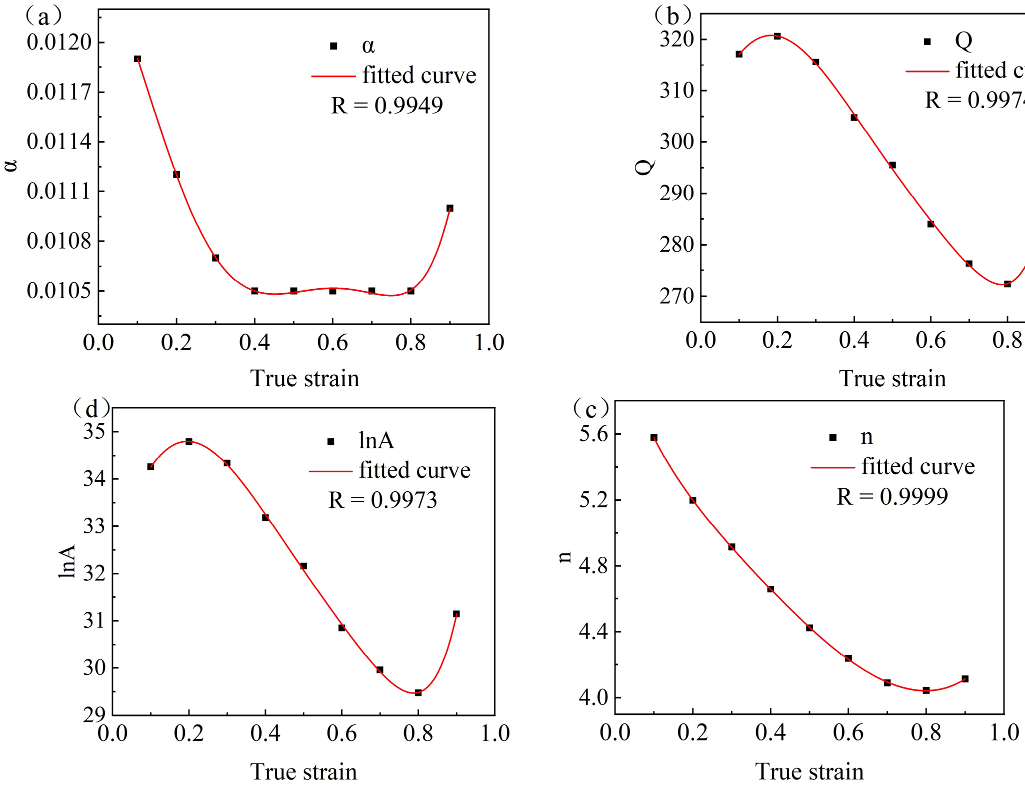

Figure 8. Fitting the variation curve with α、n、Q and ln A polynomials.

The data obtained from the experiments were substituted into Eq. (14) and the equations were fitted using a nonlinear fitting algorithm to calculate the model material constants, the results of which are shown in Table 3.

Table 3. Polynomial coefficient results for α、Q、n、ln A.

α	Q	n	ln A
0.0124	303.5464	6.1858	32.5454
-0.0017	168.8368	-7.9749	21.0176
-0.0493	-132.4121	23.8815	-17.9660
0.1819	-2689.0837	-56.1106	-292.1581
-0.2362	8011.9761	73.0744	869.1344
0.1058	-9079.7051	-48.186	-981.0780
	3772.3889	13.5021	406.9907

As a result, the Arrhenius model for strain compensation can be obtained, and the comparison between the predicted and experimental values of this model is shown in Figure 9.

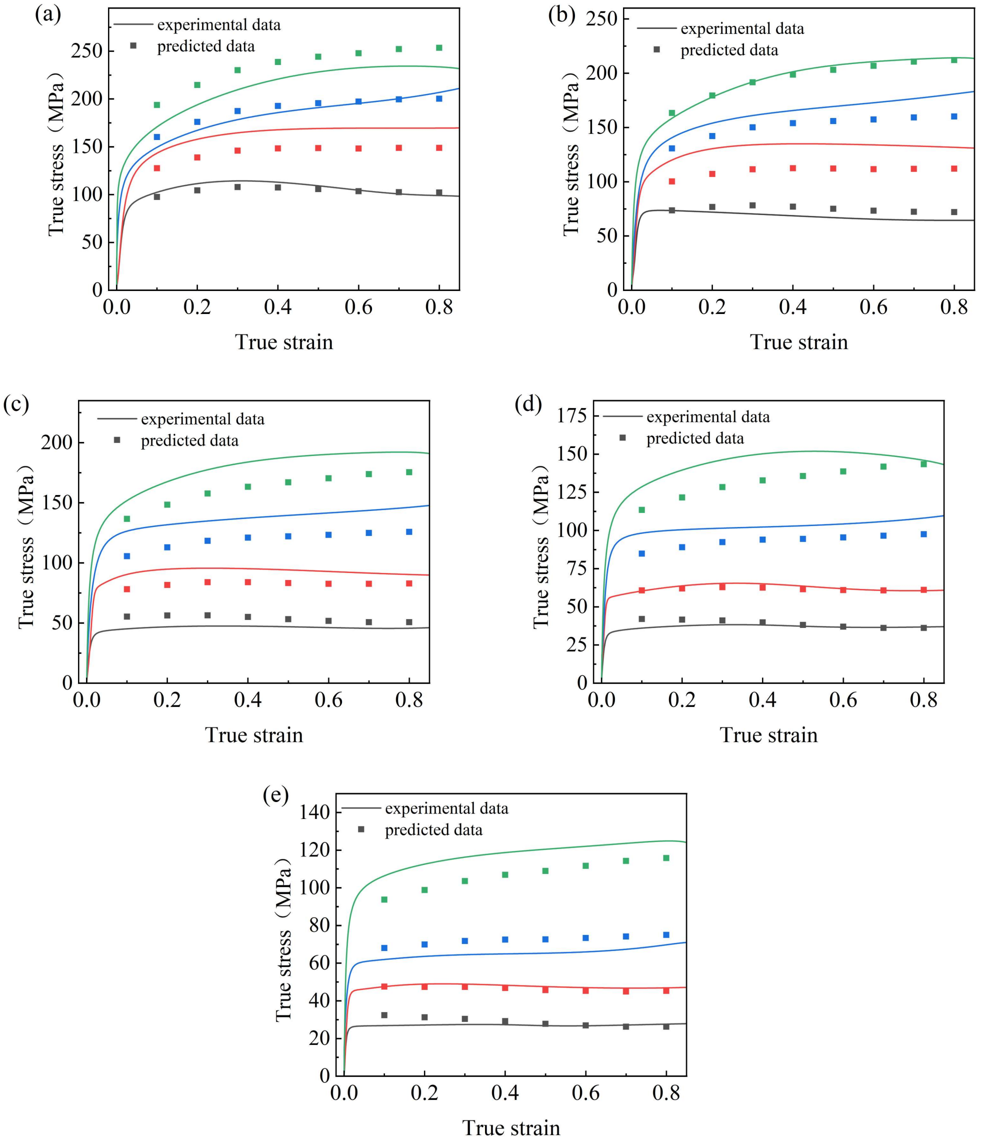

Figure 9. Comparison between experimental stress values and predicted stress values（a）933K（b）983K（c）1033K（d）1083K（e）1133K.

3.3. Evaluation of the Ontological Model

In order to be able to accurately evaluate the reliability of the predicted results of this eigenequation, it is necessary to analyze the error between the experimental values and the predicted values of the eigenequation. Here, the correlation coefficient (R), mean absolute percentage error (MAPE) and mean root mean square error (RMSE) are introduced to analyze the error numerically with the following expressions[29,30]:

$$R = \frac{\sum_{i=1}^{N} (E_i - \bar{E})(P_i - \bar{P})}{\sqrt{\sum_{i=1}^{N} (E_i - \bar{E})^2 \sum_{i=1}^{N} (P_i - \bar{P})^2}} \quad (15)$$

$$MAPE(\%) = \frac{l}{N} \sum_{i=1}^{N} \left| \frac{E_i - P_i}{E_i} \right| \times 100\% \quad (16)$$

$$RMSE = \sqrt{\frac{I}{N}\sum_{i=1}^{N}(E_i - P_i)^2} \tag{17}$$

In the above equation E_i experimental stress value; P_i predicted stress value; $\bar{E}$ is the average of experimental and predicted values; N is the total amount of data. In general, the strength of the linear correlation between the model predicted data and the experimental measured data can be characterized by the correlation coefficient (R). However, for this intrinsic model, it is not always valid to rely solely on the correlation coefficient to characterize the correlation between the model data and the experimental data. Therefore, the mean absolute percentage error (MAPE) and the mean root mean square error (RMSE) need to be calculated here to accurately characterize the accuracy of the eigenequations with unbiased statistical parameters. In order to explore the generalization ability of the proposed model, the corresponding MAPE and RMSE values were calculated and the linear relationship between the experimental values of the flow stresses and the predicted values of the model were plotted as shown in Figure 10.

From the figure, it can be seen that the MAPE and RMSE values of the model are 8.7210% and 11.0635 MPa, respectively. The data values at the whole temperature are around the optimal regression line, which can indicate that the intrinsic model has a high accuracy. This indicates that the developed TA4 Arrhenius eigen structural equation has good accuracy and its correlation is high enough to be used in the calculation of deformation resistance for the actual rolling process[31].

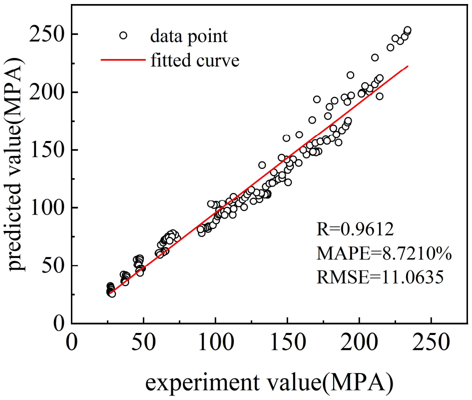

Figure 10. The correlation between experimental and predicted values.

3.4. Creation and Analysis of Thermal Processing Diagrams

In actual production, to select the appropriate thermal processing parameters for TA4 alloy, it is necessary not only to construct the constitutive equations, but also to establish the corresponding thermal processing diagram to visualize the processing and forming properties of the material. The hot working diagram can delineate the safety zone and rheological instability zone of plastic processing, which can provide guidance for the selection of hot working process parameters and the control of microstructure and properties of metal materials.

Based on Prasad's[32] instability criterion criterion and its dynamic material model, the external energy P is mainly consumed in the dissipation G required for plastic deformation and the co-dissipation J required for microstructure evolution, whose expression (18) is given below.

$$P = \sigma\dot{\varepsilon} = G + J = \int_0^{\varepsilon}\sigma d\dot{\varepsilon} + \int_0^{\sigma}\dot{\varepsilon} d\sigma \tag{18}$$

Where m is the strain rate sensitivity factor with the following expression (19); η is the power dissipation factor of the processed material with the following expression (20).

$$m = \frac{\partial \ln \sigma}{\partial \ln \dot{\varepsilon}} \tag{19}$$

$$\eta = 2\left(1 - \frac{1}{1+\mathrm{m}}\right) = \frac{2\mathrm{m}}{1+\mathrm{m}} \tag{20}$$

When the material presents an ideal linear dissipative state, the value of the strain rate sensitivity index m is 1, at which time the dissipation coefficient J reaches its maximum value J_{max}, expressed as:

$$J_{max} = \frac{\sigma\dot{\varepsilon}}{2} \tag{21}$$

Therefore, the energy dissipation rate η can be expressed as:

$$\eta = \frac{J}{J_{max}} = \frac{2m}{m+1} \tag{22}$$

In the above equation m is the strain rate sensitivity index; η is the energy dissipation rate; ξ is the destabilization parameter, when the destabilization parameter is less than 0 to judge the occurrence of rheological destabilization, the expression (21) is as follows.

$$\xi(\dot{\varepsilon}) = \frac{\partial \ln\left(\frac{\mathrm{m}}{\mathrm{m}+1}\right)}{\partial \ln \dot{\varepsilon}} + \mathrm{m} < 0 \tag{23}$$

Using different strains of the rheological instability parameter ξ value plotted as a contour map that is the instability map, and superimposed with the energy dissipation map can be made of the thermal processing map. The contour lines in the map represent the values of energy dissipation efficiency factor; the shaded area in the map represents the part where the instability parameter ξ is less than zero, i.e., the plastic rheological instability region. The thermal processing diagram of TA4 titanium alloy at different real strains is shown in Figure 11. The destabilization region at strain 0.3 is, 933~1023K, 0.01~4s^{-1}. At strain 0.6, 933~1023K, 0.02~7s^{-1}. In this strain interval, the destabilization zone gradually moves to the high strain rate interval with the increase of strain, but the overall change of the destabilization zone is small. Among them, at strain 0.9, 933~1023K, 0.04~10s^{-1}, the area of the destabilization zone increased compared to the low strain. With the increase of strain, the area of instability is gradually shifted from the location of low strain rate to the area of high strain rate, and is gradually extended from the low-temperature region to the high-temperature region. Overall, the area of the destabilized region increases with the increase of strain.

The optimum processing region is divided into two regions: the medium temperature low strain region A and the high temperature high strain region B. Region B should be avoided when designing the thermal processing parameters due to the high temperature and strain rate required. It can be seen that the energy dissipation efficiency factor is closely related to the deformation temperature and strain rate, which increases and then decreases with the rise of temperature and strain rate. The maximum region of energy dissipation efficiency factor is located in the region of medium temperature and low strain rate, and the maximum value is near 0.44. The maximum value is around 0.44. At a strain of 0.9: 1040~1133K, 0.01~0.08 s^{-1}. If the strain is 0.6, 940~1000K, 0.01~0.04 s^{-1}. At a strain of 0.3, 940~1000K, 0.01~0.08 s^{-1}.

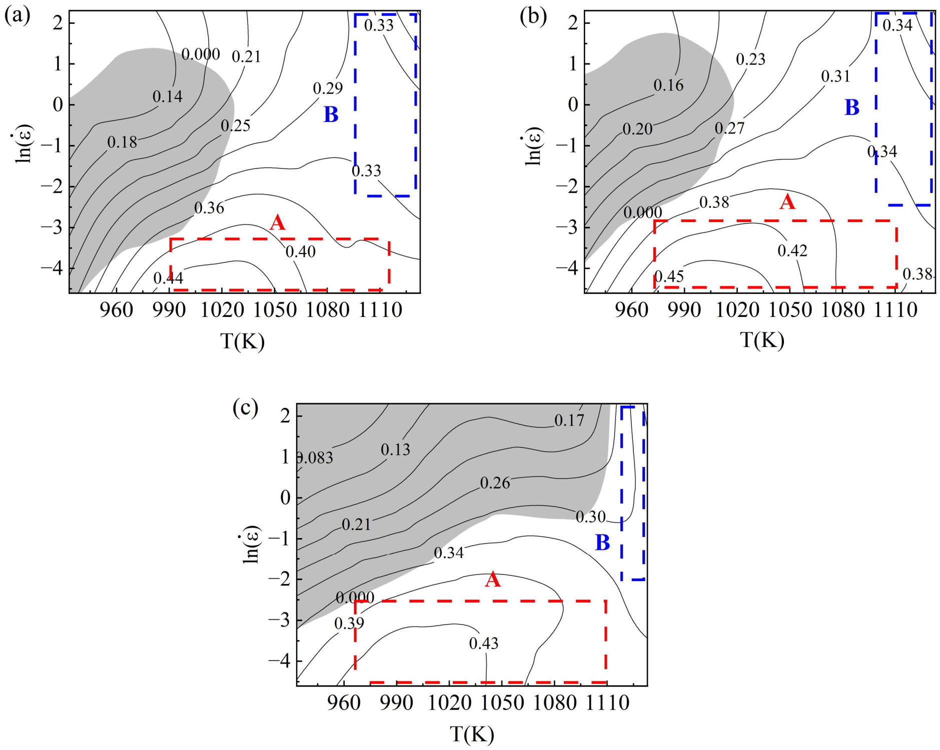

Figure 11. Hot working diagram of TA4 alloy under different strains (a)ε=0.3(b)ε=0.6(c)ε=0.9.

4. Discussion

It is difficult to elucidate the specific deformation mechanism of TA4 titanium alloy based on the stress-strain curves and thermal processing diagrams alone. In order to further investigate the effects of different thermal deformation parameters on the thermal deformation mechanism of TA4 titanium alloy, its compression samples at different temperatures at the same strain rate (1s^{-1}) and at the same temperatures (1033 K) at different strain rates were subjected to EBSD analysis.

Figure 12 shows the grain size statistics of titanium alloy under different deformation parameters. From the figure, it can be seen that the average grain area of the alloy increases significantly with the decrease of the deformation rate, from 50.23 μm^2 to 89.64 μm^2, and the grain shape tends to be more isometric. The orientation difference distribution graph indicates the proportion of grain boundary orientation angle, and Figure 13 shows the orientation difference angle distribution of titanium alloy under different deformation parameters. The blue line in the figure represents the large-angle grain boundaries (HAGBs) with dislocation angles greater than 15°, and the red line represents the small-angle grain boundaries (LAGBs) with dislocation angle angles ranging from 2° to 15°. It can be seen that with the decrease of the deformation rate, the percentage of LAGBs decreases significantly from 42. 5% to 29.8%. The original small-angle grain boundaries formed by dislocations are transformed into large-angle grain boundaries due to the process of new grain generation and growth caused by the prolongation of deformation time with DRX. It is shown that the main thermal deformation mechanism of TA4 titanium alloy at low strain rate is DRX.

In Figure 12, it can be seen that the average grain area of titanium alloy increases with the increase of deformation temperature. The average grain area increases slightly from 37.17 μm^2 to 37.77 μm^2 when rising from a low temperature of 933 K to a high temperature of 1083 K, and the grain shape does not change much. When the heating temperature rises from 1083K to 1113K, the average grain area increases significantly from 37.17μm^2 to 49.49μm^2, and the elongated grains to the equiaxial transformation trend. DRX is usually accompanied by significant changes in grain area, especially at high temperatures accompanied by grain recrystallization and grain growth process.

DRV is the recovery process of the original grains, and the grain morphology remains relatively stable in this process. The process of grain morphology remains relatively stable, grain size changes are not obvious[33]. In Figure 13 found that when the heating temperature from the low temperature 933K to high temperature 1083K when the titanium alloy LAGBs accounted for a slight increase, from 47.8% to 48.4%. When the temperature increases from 1083 K to 1113 K, the percentage of LAGBs starts to decrease, from 48.4% to 40.6%. In the DRX process nascent recrystallized grains only partially or even no LAGBs exist, and the boundaries between small grains will be reorganized by atomic diffusion during grain growth, resulting in the reduction of LAGBs, and a large portion of the LAGBs are generated in the DRV process[34]. This means that the main thermal deformation mechanism during the heating of TA4 titanium alloy from low temperature (933K) to high temperature (1083K) is DRV, which leads to little change in grain size and a slight increase in the percentage of LAGBs. When the temperature is above 1083K, the main thermal deformation mechanism is DRX, resulting in a significant increase in grain size and a decrease in the percentage of LAGBs.

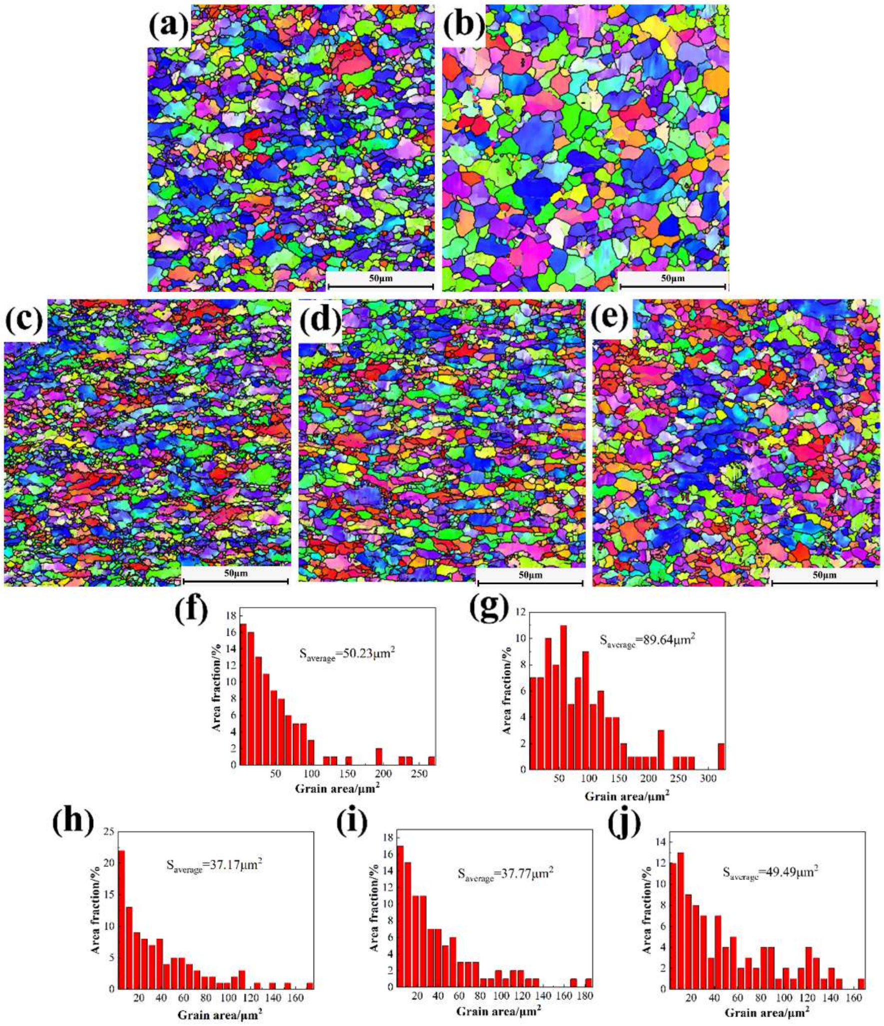

Figure 12. Deformed alloy grain sizes: (a) and (f) 1033 K/0.1s^{-1}, (b) and (g) 1033 K/0.01s^{-1}, (c) and (h) 933 K/1s^{-1}, (d) and (i) 1083 K/1s^{-1}, (e) and (j) 1133 K/1$s^{-1.}$

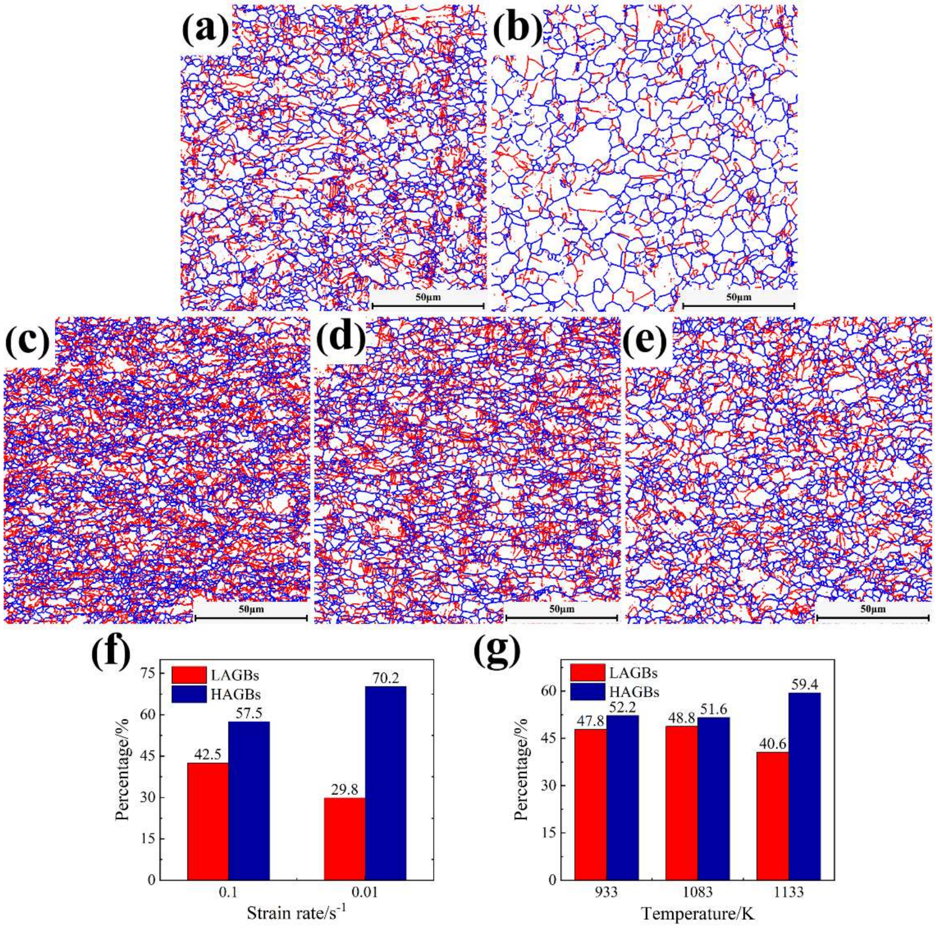

Figure 13. Grain boundary ratio of titanium alloy with different parameters: (a)1033K/0.1s^{-1}、(b)1033K/0.01s^{-1}、(c)933K/1s^{-1}、(d)1083K/1s^{-1}、(e)1133K/1s^{-1} (f) and (g) size Angle grain boundary ratio.

To further discuss the thermal deformation mechanism of TA4 titanium alloy, the percentage of dynamically recrystallized grains, substructures, and deformed grains in the typical characteristic regions of TA4 titanium alloy were counted using the grain orientation spread (GOS) parameter as shown in Figure 14. In these microstructures, grains with GOS ≤ 2° are considered as recrystallized grains and are marked in blue color. grains with GOS > 7° are deformed grains and are marked in red color. grains with 2° < GOS ≤ 7° are substructured and are marked in yellow color. In Figure 15, some equiaxed grains surrounded by HAGBs appear in the low dislocation region, which can be identified as recrystallized grains produced by the DRX process in accordance with Figure 14. There are also some irregularly shaped grains surrounded by LAGBs, which are sub-structures, and these grains are usually caused by the DRV process[35].

It can be found in Figure 14 that the percentage of recrystallized grains increases significantly from 18.4% to 36.6% with the decrease of strain rate, and the percentage of substructures decreases from 66. 5% to 60. 5%. This indicates that a considerable portion of the substructure is transformed into recrystallized grains at this time, and this phenomenon is a hallmark feature of dynamic recrystallization. It is also noted that 1033K0.01s^{-1} is in the optimal processing zone A of Figure 11, when the grain size is the largest, the percentage of recrystallization is the largest, and the average orientation difference is the lowest value of only 0.49, which indicates that it has a better processing performance and is in agreement with the results obtained from the thermal processing diagram. When the deformation temperature is gradually increased, the percentage of both recrystallization and substructure increases. However, it is worth noting that when the temperature increases from 933 K to 1083 K, the percentage of recrystallization only increases from 14.1% to 14.4%, and the percentage of substructure increases significantly from 45.9% to 61.8%. And from Figure 15, we see that the dislocation dislocation density decreases significantly at this time, the average value changes from 1.06 to 0.86, and the KAM value near the grain boundary is larger than that in the grain. This indicates that a large number of dislocations generated inside the grains during the deformation process are rearranged and reorganized under the influence of DRV to form small-angle grain boundaries, which are also known as subgranular boundaries, and the most sub-structures surrounded by LAGBs are formed. At the same time, DRV is more likely to affect the dislocations inside the grains to slip, climb and annihilate, which leads to a relatively low KAM value inside the grains. When the temperature increases from 1083 K to 1133 K, the percentage of recrystallization increases from 14.4% to 22%, the percentage of substructure increases from 61.8% to 67%, and the percentage of deformed grains decreases from 23.8% to 11%. And the overall dislocation density increases at this time, the average value changes from 1.06 to 0.86, and the KAM value inside the grain boundary is larger than that near the grain boundary. This indicates that the increase in the percentage of recrystallized grains, the formation of new grains at grain boundaries and the consumption of dislocations at grain boundaries at high temperatures suggests that dynamic recrystallization has occurred near grain boundaries. However, the overall rise in dislocations indicates that it is at this point in the process of recrystallized nucleation generation at the initial stage of DRX[36].

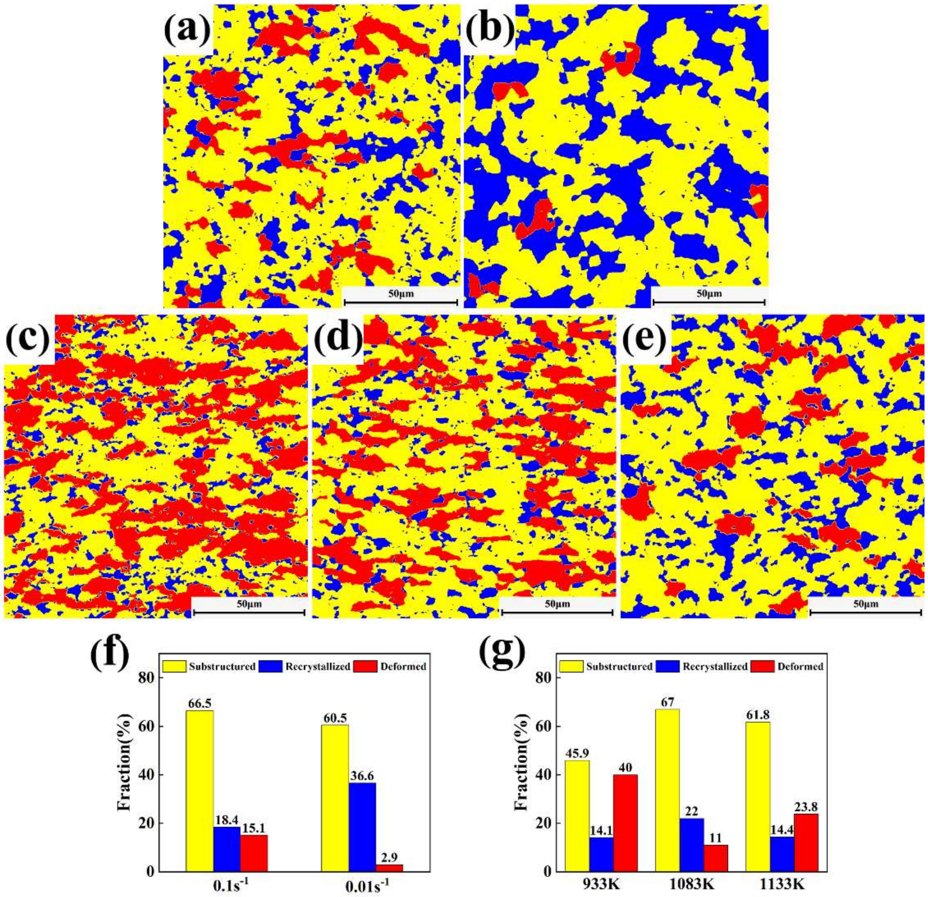

Figure 14. Recrystallization, substructure and deformation grain of the alloy with different parameters: (a)1033K/0.1s^{-1}、(b)1033K/0.01s^{-1}、(c)933K/1s^{-1}、(d)1083K/1s^{-1}、(e)1133K/1s^{-1} (f) and (g) the proportion of different grain types.

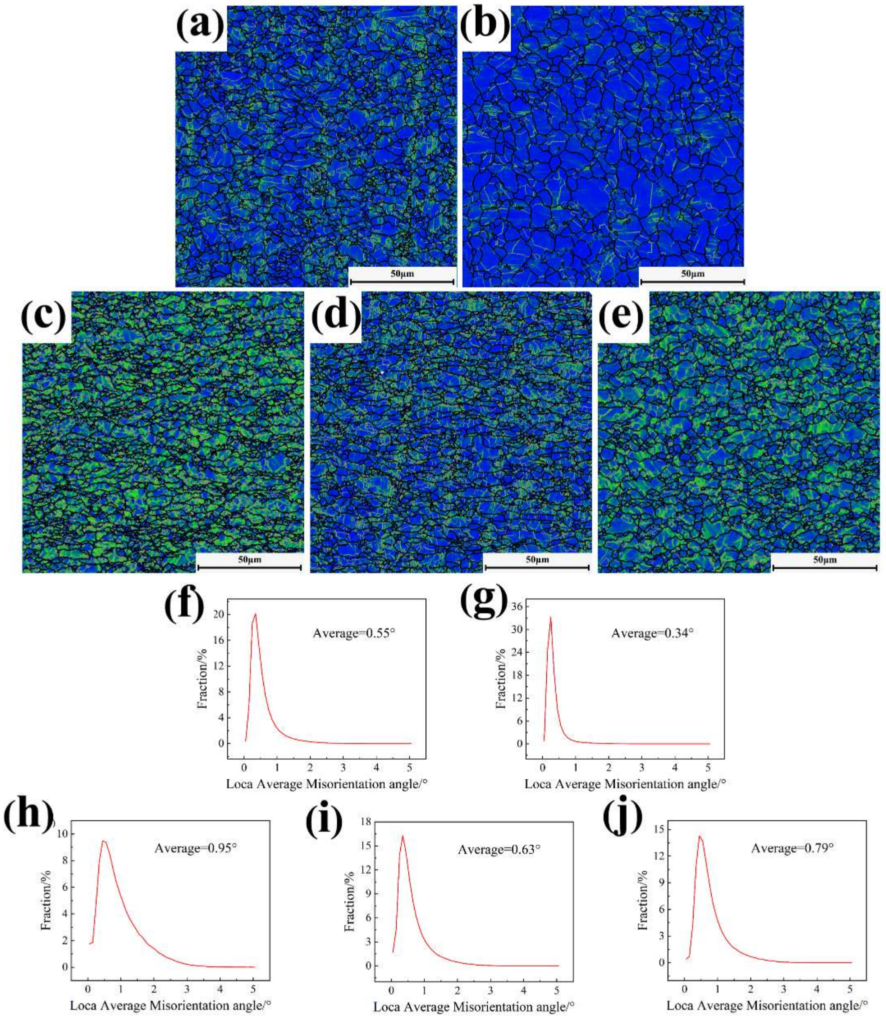

Figure 15. KAM distributions: (a) and (f) 1033 K/0.1s^{-1}, (b) and (g) 1033 K/0.01s^{-1}, (c) and (h) 933 K/1s^{-1}, (d) and (i) 1083 K/1s^{-1}, (e) and (j) 1133 K/1s$^{-1.}$

5. Conclusions

In this paper, isothermal compression tests were carried out on TA4 titanium alloy specimens using a Gleeble-3800 thermal simulation testing machine to study the thermal deformation behavior of TA4 titanium alloy. By analyzing the strain-stress-strain curves obtained from the tests and using the strain-compensated Arrhenius model, the thermo-compression eigenstructure equations and thermal processing diagrams of TA4 titanium alloy are constructed. And the following conclusions were drawn:

(1) In the heat deformation behavior, the flow stress of TA4 titanium alloy decreases with the increase of the deformation temperature or the decrease of the strain rate, and the stress-strain curve in general shows the law of rapid increase and finally stabilization.

(2) The constitutive equation based on the strain-compensated Arrhenius model was established for TA4 titanium alloy. After analyzing, the correlation coefficient between the predicted and experimental values of this constitutive model is 0.9612, the average absolute percentage error is 8.7210%, and the average root-mean-square error is 11.0635 MPa, which indicates that this constitutive equation has a better prediction ability for the rheological stresses in the temperature interval of 933-1133 K and the interval of strain rate of 0.01-10 s^{-1} for TA4 titanium alloy.

(3) The optimal processing region of TA4 titanium alloy is mainly divided into two regions, in which the region with the largest energy dissipation efficiency factor is located in the region of medium temperature and low strain rate, with the maximum value of 0.44. The optimal processing region with the larger energy dissipation efficiency factor is as follows at different strains: at a strain of 0.9: 1040~1133K, 0.01~0.7 s^{-1}. At a strain of 0.6, the optimal processing region is 940~1000K, 0.01~0.04 s^{-1}. At a strain of 0.3, 940~1000K, 0.01~0.08 s^{-1}. 1000K, 0.01~0.04 s^{-1}. At a strain of 0.3 940~1000K, 0.01~0.08 s^{-1}.

(4) The main deformation softening mechanism of TA4 titanium alloy during thermal deformation is DRV at low temperature and high strain rate, DRX at high temperature and high strain rate, and DRX at low strain rate.

CRediT authorship contribution statement: Lifeng Ma: Writing – original draft, Investigation, Data curation. Wenshuai Liu: Writing – review & editing, Data curation, Formal analysis. Yanchun Zhu: Writing – review & editing, Data curation, Formal analysis. Ling Qin: Writing – review & editing, Data curation, Funding acquisition, Conceptualization. Jingfeng Zou: Validation, Data curation.

Declaration of competing interest: The authors declare that they have no known competing financial interests or personal relationships that could have appeared to influence the work reported in this paper.

Acknowledgements: This work was supported by the National Natural Science Foundation of China (No. 52375363), (No. B2408100.W12), (No. 52205400) and (No. 52375362), the Applied Basic Research Project of Shanxi Province (No. 202203021211208), Technological Innovation Talent Team Special Plan of Shanxi Province (202204051002002).

Data availability: Data will be made available on request.

References

1. Wang, Z.B.; Hu, H.X.; Zheng, Y.G.; Ke, W.; Qiao, Y.X. Comparison of the corrosion behavior of pure titanium and its alloys in fluoride-containing sulfuric acid. *Corrosion Science* **2016**, *103*, 50-65, doi:10.1016/j.corsci.2015.11.003.
2. Shahmir, H.; Pereira, P.H.R.; Huang, Y.; Langdon, T.G. Mechanical properties and microstructural evolution of nanocrystalline titanium at elevated temperatures. *Materials Science and Engineering: A* **2016**, *669*, 358-366, doi:10.1016/j.msea.2016.05.105.
3. Niu, Y.; Hong, Z.-q.; Wang, Y.-q.; Zhu, Y.-c. Machine learning-based beta transus temperature prediction for titanium alloys. *Journal of Materials Research and Technology* **2023**, *23*, 515-529, doi:10.1016/j.jmrt.2023.01.019.
4. Fan, X.G.; Yang, H.; Gao, P.F. Prediction of constitutive behavior and microstructure evolution in hot deformation of TA15 titanium alloy. *Materials & Design* **2013**, *51*, 34-42, doi:10.1016/j.matdes.2013.03.103.
5. Momeni, A.; Abbasi, S.M. Effect of hot working on flow behavior of Ti–6Al–4V alloy in single phase and two phase regions. *Materials & Design* **2010**, *31*, 3599-3604, doi:10.1016/j.matdes.2010.01.060.
6. Yang, Y.; Xu, D.; Cao, S.; Wu, S.; Zhu, Z.; Wang, H.; Li, L.; Xin, S.; Qu, L.; Huang, A. Effect of strain rate and temperature on the deformation behavior in a Ti-23.1Nb-2.0Zr-1.0O titanium alloy. *Journal of Materials Science & Technology* **2021**, *73*, 52-60, doi:10.1016/j.jmst.2020.09.030.
7. Yu, J.; Li, Z.; Qian, C.; Huang, S.; Xiao, H. Investigation of deformation behavior, microstructure evolution, and hot processing map of a new near-α Ti alloy. *Journal of Materials Research and Technology* **2023**, *23*, 2275-2287, doi:10.1016/j.jmrt.2023.01.177.
8. Wang, X.; Liu, P.; Liang, C.; Lu, T.; Feng, T.; Niu, H.; Dong, Y.; Liu, X. Investigation on the thermal deformation mechanisms and constitutive model of Ti-55511 titanium alloy. *Journal of Materials Research and Technology* **2024**, *33*, 6780-6797, doi:10.1016/j.jmrt.2024.11.057.
9. Li, L.; Ma, G.; Huang, H.; Xiao, H.; Yuan, Z.; Li, Y.; Zhou, R. Flow behavior analysis and prediction of flow instability of a lamellar TA10 titanium alloy. *Materials Characterization* **2022**, *194*, doi:10.1016/j.matchar.2022.112403.

10. Abbasi, S.M.; Momeni, A.; Lin, Y.C.; Jafarian, H.R. Dynamic softening mechanism in Ti-13V-11Cr-3Al beta Ti alloy during hot compressive deformation. *Materials Science and Engineering: A* **2016**, *665*, 154-160, doi:10.1016/j.msea.2016.04.040.
11. Xiang, Y.; Xiang, W.; Yuan, W. Flow softening and microstructural evolution of near β titanium alloy Ti-55531 during hot compression deformation in the α + β region. *Journal of Alloys and Compounds* **2023**, *955*, doi:10.1016/j.jallcom.2023.170165.
12. Priyadarshi, A.; Shahrani, S.B.; Choma, T.; Zrodowski, L.; Qin, L.; Leung, C.L.A.; Clark, S.J.; Fezzaa, K.; Mi, J.; Lee, P.D. New insights into the mechanism of ultrasonic atomization for the production of metal powders in additive manufacturing. *Additive Manufacturing* **2024**, *83*, 104033, doi:10.1016/j.addma.2024.104033.
13. Xiang, K.; Qin, L.; Zhao, Y.; Huang, S.; Du, W.; Boller, E.; Rack, A.; Li, M.; Mi, J. Operando study of the dynamic evolution of multiple Fe-rich intermetallics of an Al recycled alloy in solidification by synchrotron X-ray and machine learning. *Acta Materialia* **2024**, *279*, 120267, doi:10.1016/j.actamat.2024.120267.
14. Qin, L.; Du, W.; Cipiccia, S.; Bodey, A.J.; Rau, C.; Mi, J. Synchrotron X-ray operando study and multiphysics modelling of the solidification dynamics of intermetallic phases under electromagnetic pulses. *Acta Materialia* **2024**, *265*, 119593, doi:10.1016/j.actamat.2023.119593.
15. Qin, L.; Zhang, Z.; Guo, B.; Li, W.; Mi, J. Determining the Critical Fracture Stress of Al Dendrites near the Melting Point via Synchrotron X-ray Imaging. *Acta Metallurgica Sinica (English Letters)* **2023**, *36*, 857-864, doi:10.1007/s40195-023-01531-w.
16. Zhang, Z.; Khong, J.C.; Koe, B.; Luo, S.; Huang, S.; Qin, L.; Cipiccia, S.; Batey, D.; Bodey, A.J.; Rau, C. Multiscale characterization of the 3D network structure of metal carbides in a Ni superalloy by synchrotron X-ray microtomography and ptychography. *Scripta Materialia* **2021**, *193*, 71-76, doi:10.1016/j.scriptamat.2020.10.032.
17. Huang, S.; Luo, S.; Qin, L.; Shu, D.; Sun, B.; Lunt, A.J.; Korsunsky, A.M.; Mi, J. 3D local atomic structure evolution in a solidifying Al-0.4 Sc dilute alloy melt revealed in operando by synchrotron X-ray total scattering and modelling. *Scripta Materialia* **2022**, *211*, 114484, doi:10.1016/j.scriptamat.2021.114484.
18. Zhang, Y.; Huang, T.; Zhou, Z.; Li, M.; Tan, L.; Gan, B.; Jie, Z.; Qin, L.; Zhang, J.; Liu, L. Variation of Homogenization Pores during Homogenization for Nickel-Based Single-Crystal Superalloys. *Advanced Engineering Materials* **2021**, *23*, 2001547, doi:10.1002/adem.202001547.
19. Xie, H.; Wang, J.; Li, Y.; Song, J.; Hu, H.; Qin, L.; Zhao, H.; Li, C.; Cui, Y.; Tan, Z.; et al. Fast shot speed induced microstructure and mechanical property evolution of high pressure die casting Mg-Al-Zn-RE alloys. *Journal of Materials Processing Technology* **2024**, *331*, doi:10.1016/j.jmatprotec.2024.118523.
20. Huang, H.; Qin, L.; Tang, H.; Shu, D.; Yan, W.; Sun, B.; Mi, J. Ultrasound cavitation induced nucleation in metal solidification: An analytical model and validation by real-time experiments. *Ultrasonics Sonochemistry* **2021**, *80*, 105832, doi:10.1016/j.ultsonch.2021.105832.
21. Han, L.; Zhang, H.; Cheng, J.; Zhou, G.; Wang, C.; Chen, L. Thermal Deformation Behavior of Ti-6Mo-5V-3Al-2Fe Alloy. *Crystals* **2021**, *11*, 1245, doi:10.3390/cryst11101245.
22. Chai, Y.; Zhu, Y.; Qin, L.; Luo, Y.; Niu, Y.; Shao, Z. High-temperature hot deformation behavior and processing map of Ti-22Al-25Nb alloy. *Materials Today Communications* **2024**, *41*, 110599, doi:10.1016/j.mtcomm.2024.110599.
23. Shokry, A.; Gowid, S.; Kharmanda, G. An improved generic Johnson-Cook model for the flow prediction of different categories of alloys at elevated temperatures and dynamic loading conditions. *Materials Today Communications* **2021**, *27*, doi:10.1016/j.mtcomm.2021.102296.
24. Zhao, Y.; Sun, J.; Li, J.; Yan, Y.; Wang, P. A comparative study on Johnson-Cook and modified Johnson-Cook constitutive material model to predict the dynamic behavior laser additive manufacturing FeCr alloy. *Journal of Alloys and Compounds* **2017**, *723*, 179-187, doi:10.1016/j.jallcom.2017.06.251.
25. Gambirasio, L.; Rizzi, E. On the calibration strategies of the Johnson–Cook strength model: Discussion and applications to experimental data. *Materials Science and Engineering: A* **2014**, *610*, 370-413, doi:10.1016/j.msea.2014.05.006.

26. Chen, W.; Guan, Y.; Wang, Z. Modeling of Flow Stress of High Titanium Content 6061 Aluminum Alloy Under Hot Compression. *Journal of Materials Engineering and Performance* **2016**, *25*, 4081-4088, doi:10.1007/s11665-016-2224-z.
27. Liao, H.; Wu, Y.; Zhou, K.; Yang, J. Hot deformation behavior and processing map of Al–Si–Mg alloys containing different amount of silicon based on Gleebe-3500 hot compression simulation. *Materials & Design (1980-2015)* **2015**, *65*, 1091-1099, doi:10.1016/j.matdes.2014.08.021.
28. Abbasi-Bani, A.; Zarei-Hanzaki, A.; Pishbin, M.H.; Haghdadi, N. A comparative study on the capability of Johnson–Cook and Arrhenius-type constitutive equations to describe the flow behavior of Mg–6Al–1Zn alloy. *Mechanics of Materials* **2014**, *71*, 52-61, doi:10.1016/j.mechmat.2013.12.001.
29. Wang, Y.; Peng, J.; Zhong, L.; Pan, F. Modeling and application of constitutive model considering the compensation of strain during hot deformation. *Journal of Alloys and Compounds* **2016**, *681*, 455-470, doi:10.1016/j.jallcom.2016.04.153.
30. Zhou, Z.; Fan, Q.; Xia, Z.; Hao, A.; Yang, W.; Ji, W.; Cao, H. Constitutive Relationship and Hot Processing Maps of Mg-Gd-Y-Nb-Zr Alloy. *Journal of Materials Science & Technology* **2017**, *33*, 637-644, doi:10.1016/j.jmst.2015.10.019.
31. Mandal, S.; Rakesh, V.; Sivaprasad, P.V.; Venugopal, S.; Kasiviswanathan, K.V. Constitutive equations to predict high temperature flow stress in a Ti-modified austenitic stainless steel. *Materials Science and Engineering: A* **2009**, *500*, 114-121, doi:10.1016/j.msea.2008.09.019.
32. Robi, P.S.; Dixit, U.S. Application of neural networks in generating processing map for hot working. *Journal of Materials Processing Technology* **2003**, *142*, 289-294, doi:10.1016/s0924-0136(03)00579-x.
33. Hou, Z.; Liu, H.; Lu, L.; Li, W.; Zhang, Z.; Lu, W.; Feng, Q.; Jia, B.; Song, K. Effect of rare earth yttrium and the deformation process on the thermal deformation behavior and microstructure of pure titanium for cathode rolls. *Journal of Materials Research and Technology* **2024**, *33*, 4192-4205, doi:10.1016/j.jmrt.2024.10.114.
34. Wang, Y.; Li, Z.; Wang, H.; Hou, M.; Yu, K.; Xu, Y.; Xiao, H. Flow behavior and dynamic recrystallization mechanism of a new near-alpha titanium alloy Ti-0.3 Mo-0.8 Ni-2Al-1.5 Zr. *Journal of Materials Research and Technology* **2024**, *30*, 3863-3876, doi:10.1016/j.jmrt.2024.04.076.
35. Ma, L.; He, D.; Yang, B.; Han, X.; Zhang, J.; Li, W. Construction and application of a physically-based constitutive model for superplastic deformation of near-α TNW700 titanium alloy. *Journal of Materials Research and Technology* **2025**, *34*, 2071-2089, doi:10.1016/j.jmrt.2024.12.224.
36. Yang, Y.; Wang, H.; Feng, Z.; Shi, Q.; Yang, B.; Chen, M.; Qi, H.; Wang, X. Study on the warm deformation behavior and microstructure evolution of the MDIFed Ti–6Al–4V titanium alloy. *Journal of Materials Research and Technology* **2024**, *33*, 8929-8943, doi:10.1016/j.jmrt.2024.11.182.